Supplementary Information

Unraveling Lone Pair Induced Bonding Effects on Thermal Conductivity in Metal Chalcogenides using Machine Learning Potentials

Harpriya Minhas,[†] Rahul Kumar Sharma,[†] Biswarup Pathak[†,*]

[†] Department of Chemistry, Indian Institute of Technology (IIT) Indore, Indore, Madhya Pradesh, 453552, India

*E-mail: biswarup@iiti.ac.in

Contents

Text S1. Unsupervised Machine Learning

Using the *matminer* library, we extracted 150-dimensional descriptors encoding both compositional and structural attributes.[1] Highly correlated features were systematically eliminated to reduce redundancy and noise. The refined feature set was subjected to dimensionality reduction via principal component analysis (PCA), preserving the top 30 principal components that captured the majority of variance in the data.[2] These 30-dimensional representations were subsequently projected into a two-dimensional latent space using t-distributed stochastic neighbor embedding (t-SNE), which emphasizes the preservation of local neighborhood similarities.[3] To elucidate latent chemical groupings, we applied K-means clustering to the t-SNE-embedded space as represented in **Figure 1a**.[4] The optimal number of clusters was identified as K = 8, as determined by two independent approaches: the elbow method, which revealed a plateau in inertia reduction beyond K = 8, and silhouette analysis, which yielded a maximum silhouette score of 0.49 at K = 8, indicating a well-defined clustering structure (**Figure S1**).

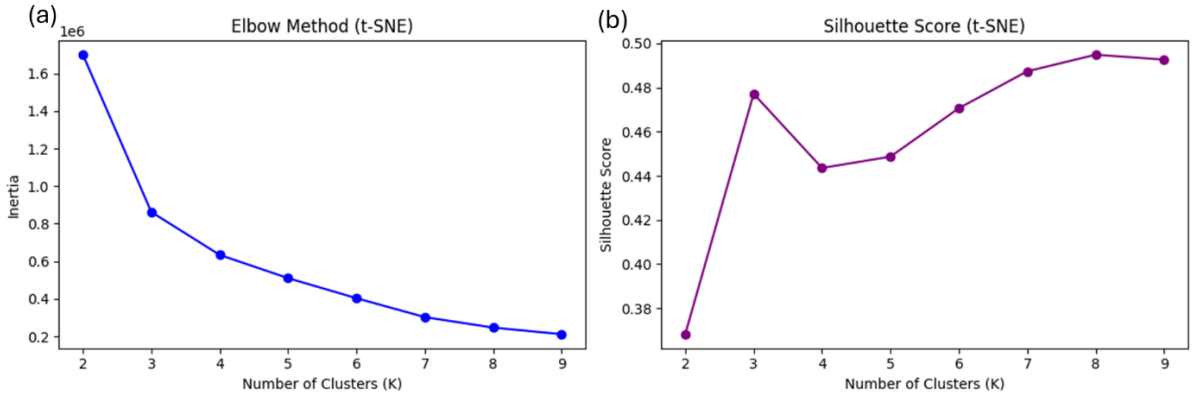

Figure S1. Determination of the optimal number of clusters using k-means clustering. **(a)** Elbow method plot showing the decrease in inertia (within-cluster sum of squares) as the number of clusters (K) increases, with the optimal K suggested at the point where the decrease begins to level off. **(b)** Silhouette score plot illustrating the average silhouette coefficient for each K, where higher values indicate better-defined clusters.

Table S1. K-means Cluster Descriptions for Pnictogen Chalcogenide (pn-chg) Systems Based on Chemical and Structural Properties

Cluster	Chemical and Structural Description
C1	Comprises alkali-metal arsenic chalcogenides enriched in s-block cations
C2	Dominated by lanthanide-centered frameworks with f-block chemistry
C3	Encompasses transition-metal-based compounds
C4	Composed of systems rich in p-block elements
C5	Features halide-chalcogenide hybrids coordinated by p-block metal centers
C6	Includes fluorinated and halogen-dense materials with anionic frameworks
C7	Contains s-block-rich compositions frequently coexisting with oxide anions
C8	Multinary systems incorporating alkali/alkaline-earth metals and lanthanides

Text S2. Universal Machine Learning Interatomic Potentials (uMLIPs)

MatterSim. The input data for the MatterSim model are constructed from material graphs built upon the underlying point clouds in the three-dimensional Euclidean space with periodic boundary conditions.[5] Each point represents an atom with an associated element from the periodic table. We define a materials graph $G = (Z,V,R,[L,S])$ with the following components: Z denotes the atomic number z_i and additional features. The geometric features are encapsulated by V and atomic coordinates R, with each atomic position r in Euclidean space R^3. V represents the relative vectors, such as the bond information between two atoms. S and L are additional optional information, where S is the global scalar state information, such as temperature, pressure, and other conditions, and L is the 3×3 lattice matrix in crystals. Within material graphs, nodes correspond to individual atoms and edges are formed based on a predefined rule. Here, a radial cutoff distance r_c is used to construct edges. For any two atoms r_i and r_j, there exists an edge if the Euclidean distance between them is less than or equal to $\leq r_c$. It should be noted that if the coordinates are fractional, we scale them to Cartesian coordinates. As a form of geometric graph, materials graphs exhibit roto-translational

symmetry in Euclidean space; specifically, MatterSim maintains roto-translational invariance for scalar properties, such as total energy of materials, and equivariance for vectorial properties like forces. Given a material graph, MatterSim adapts different input representations and crystalline features compatible with the underlying architectures, M3GNet and Graphormer.

MACE. The MACE architecture, proposed by *Batatia et al.* (2022), integrates O(3)-equivariant message passing with explicit many-body interactions to construct fast and highly accurate machine-learned interatomic potentials.[6] Unlike conventional equivariant graph neural networks that rely primarily on pairwise (two-body) messages and deep stacking to build complexity, MACE encodes higher-order (three- and four-body) correlations directly within its message-passing layers, thereby enhancing expressivity, data efficiency, and scalability. This design enables MACE to achieve state-of-the-art accuracy on benchmark datasets while maintaining computational efficiency. Notably, the introduction of many-body messages alters the empirical power-law exponent of the learning curves, leading to more rapid improvement with increasing data, whereas the inclusion of equivariance alone shifts the curves without affecting their scaling behavior. By efficiently capturing complex multi-atom interactions, MACE provides a physically grounded and computationally robust framework, particularly well-suited for modeling materials where many-body effects such as phonon scattering and thermal transport play a critical role.

CHGNet. The Crystal Hamiltonian Graph Neural Network (CHGNet) is a model pre-trained on the energies, forces, stresses, and magnetic moments from the 1.5 million crystal structures from MPtrj dataset.[7] In the CHGNet architecture, the angle information is drawn as a pairwise message passing convolution between bonds (bond graph, where bonds are nodes and edges are angles), on top of the bond information which is drawn as a pairwise convolution between atoms (atom graph, where atoms are nodes and edges are bonds).[7] To constrain the atom features used to predict energy, forces, and stresses by their charge-state information, the latter

is inferred from the magnetic moments and atomic orbital theory before the last convolution layer.

Fine-tuning and transfer learning are efficient strategies used with large pretrained deep learning models to achieve improved accuracy on small target datasets with data efficiency compared with training the model from scratch.[7–10] While the robustness of the pretrained uMLIPs has been demonstrated in the application examples, better energy and force accuracy can be achieved with fine-tuning to specific material systems if a high-precision study is desired. When fine-tuning with additional DFT data points, the effective potential energy surface described in uMLIP is adjusted to accommodate the additional data. To achieve better extrapolation and preservation of pretrained knowledge, freezing deeper layers and only allowing the shallow layers to update during fine-tuning.

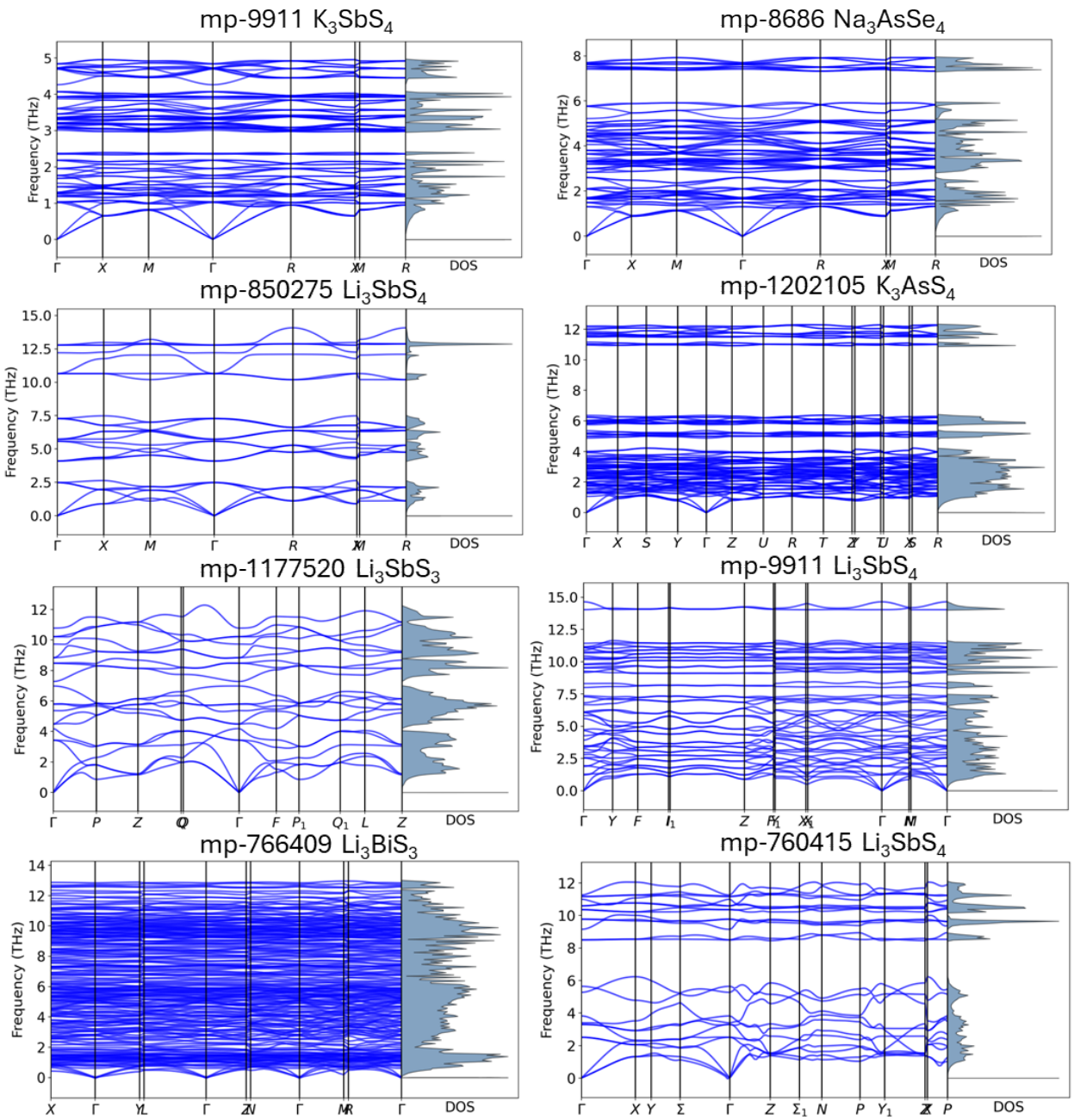

Figure S2. Phonon dispersion curves demonstrating dynamical stability of pnictogen chalcogenides from cluster C1 using MatterSim.

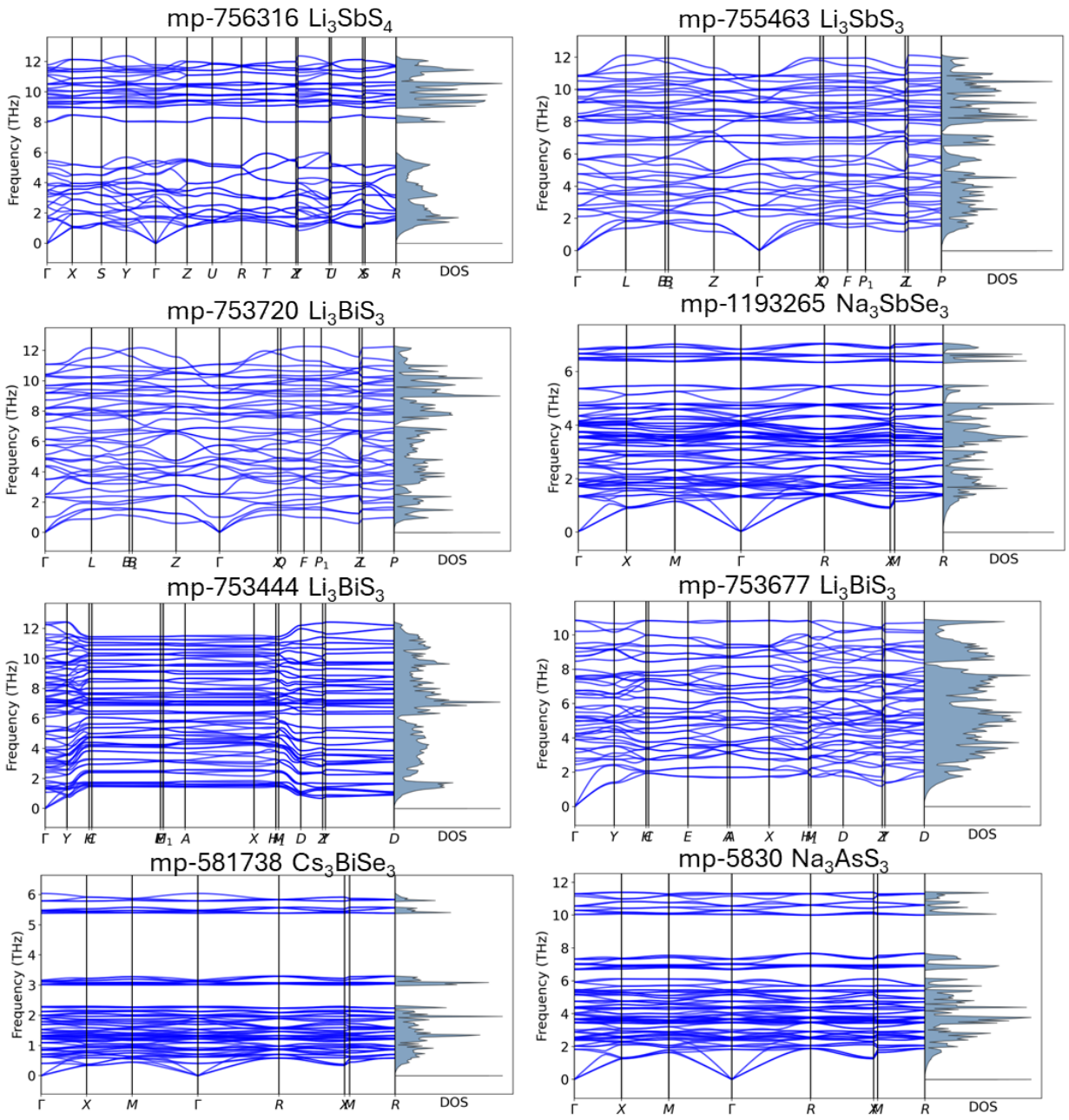

Figure S3. Phonon dispersion curves demonstrating dynamical stability of pnictogen chalcogenides from cluster C1 using MatterSim.

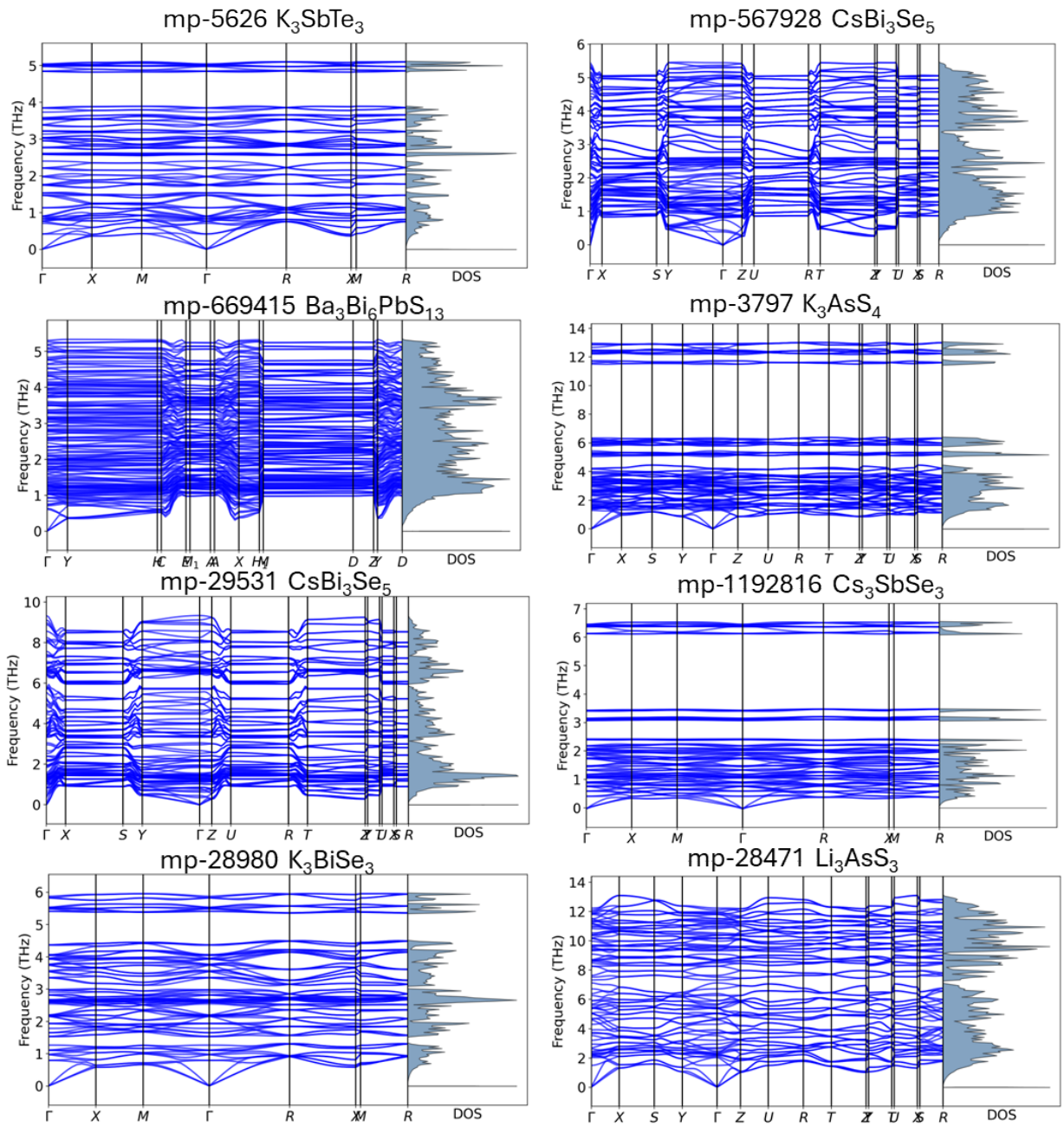

Figure S4. Phonon dispersion curves demonstrating dynamical stability of pnictogen chalcogenides from cluster C1 using MatterSim.

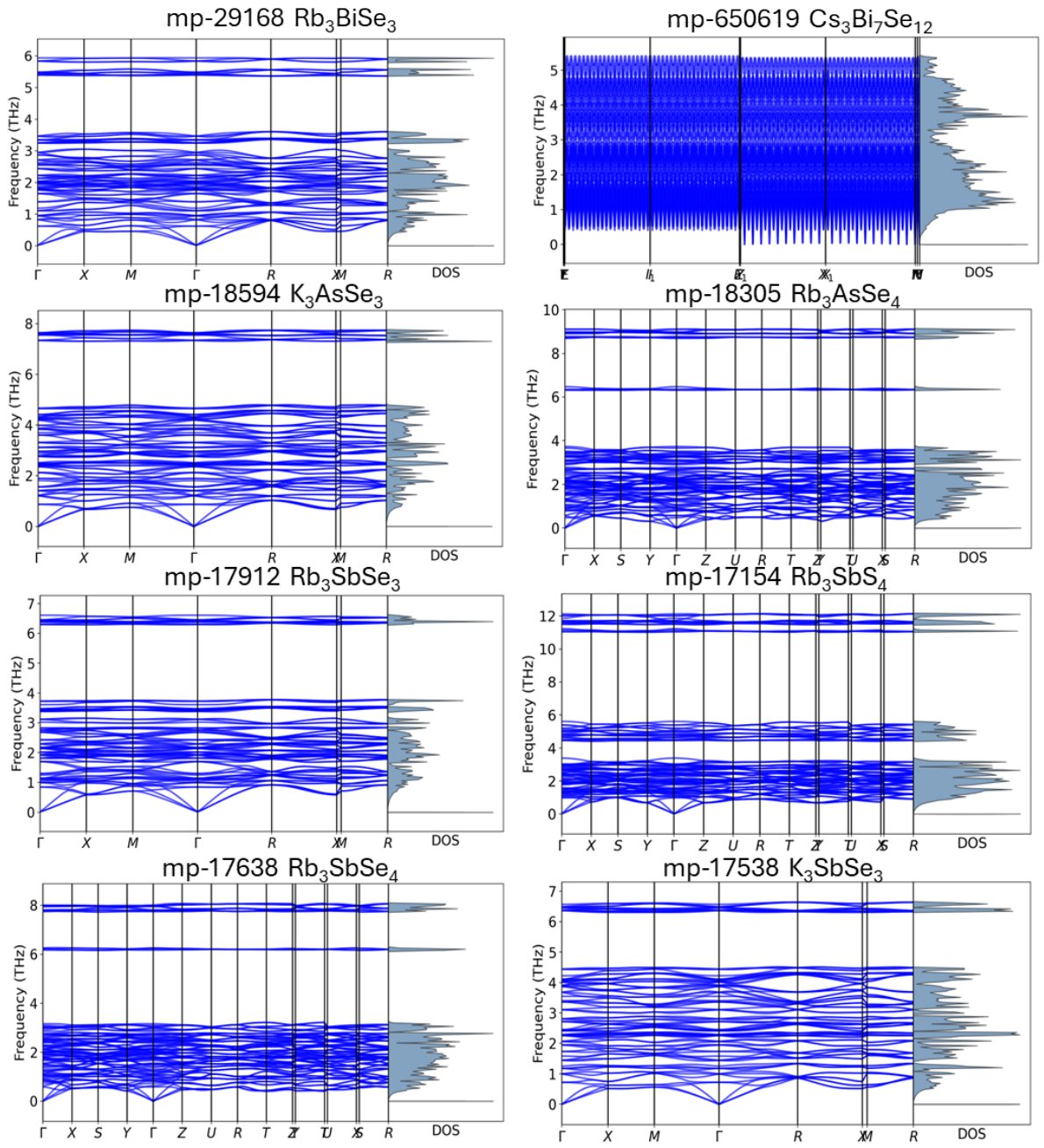

Figure S5. Phonon dispersion curves demonstrating dynamical stability of pnictogen chalcogenides from cluster C1 using MatterSim.

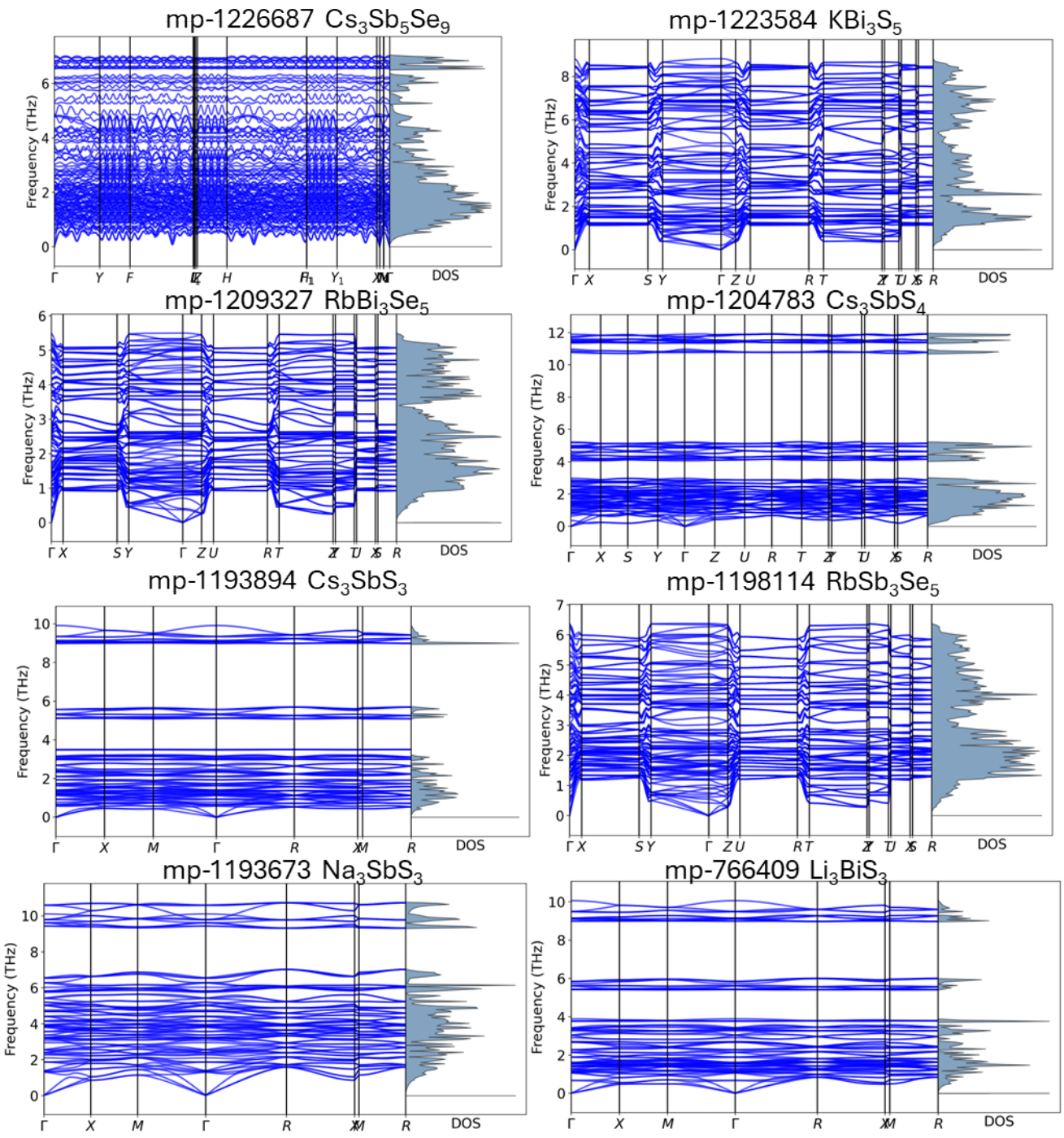

Figure S6. Phonon dispersion curves demonstrating dynamical stability of pnictogen chalcogenides from cluster C1 using MatterSim.

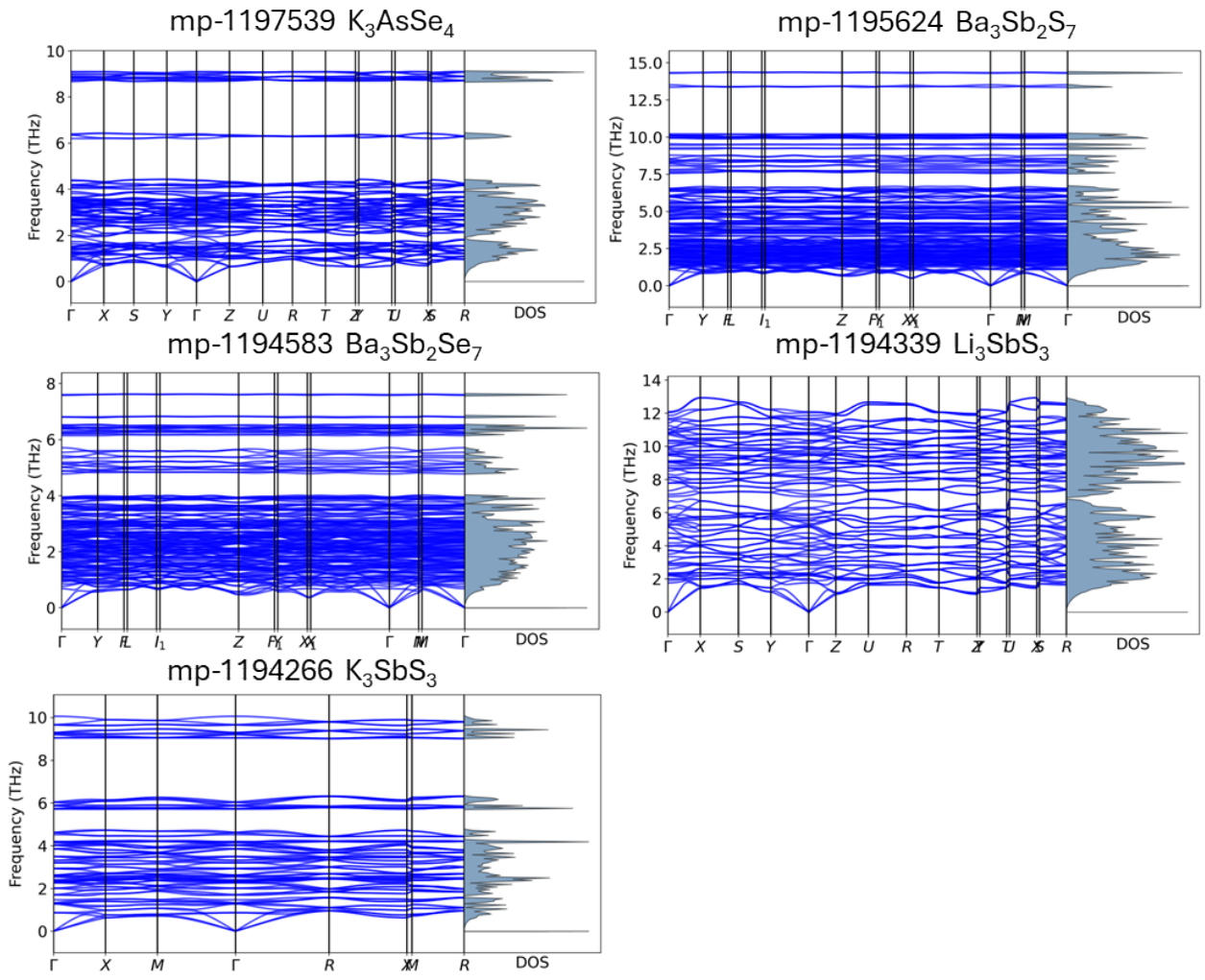

Figure S7. Phonon dispersion curves demonstrating dynamical stability of pnictogen chalcogenides from cluster C1 using MatterSim.

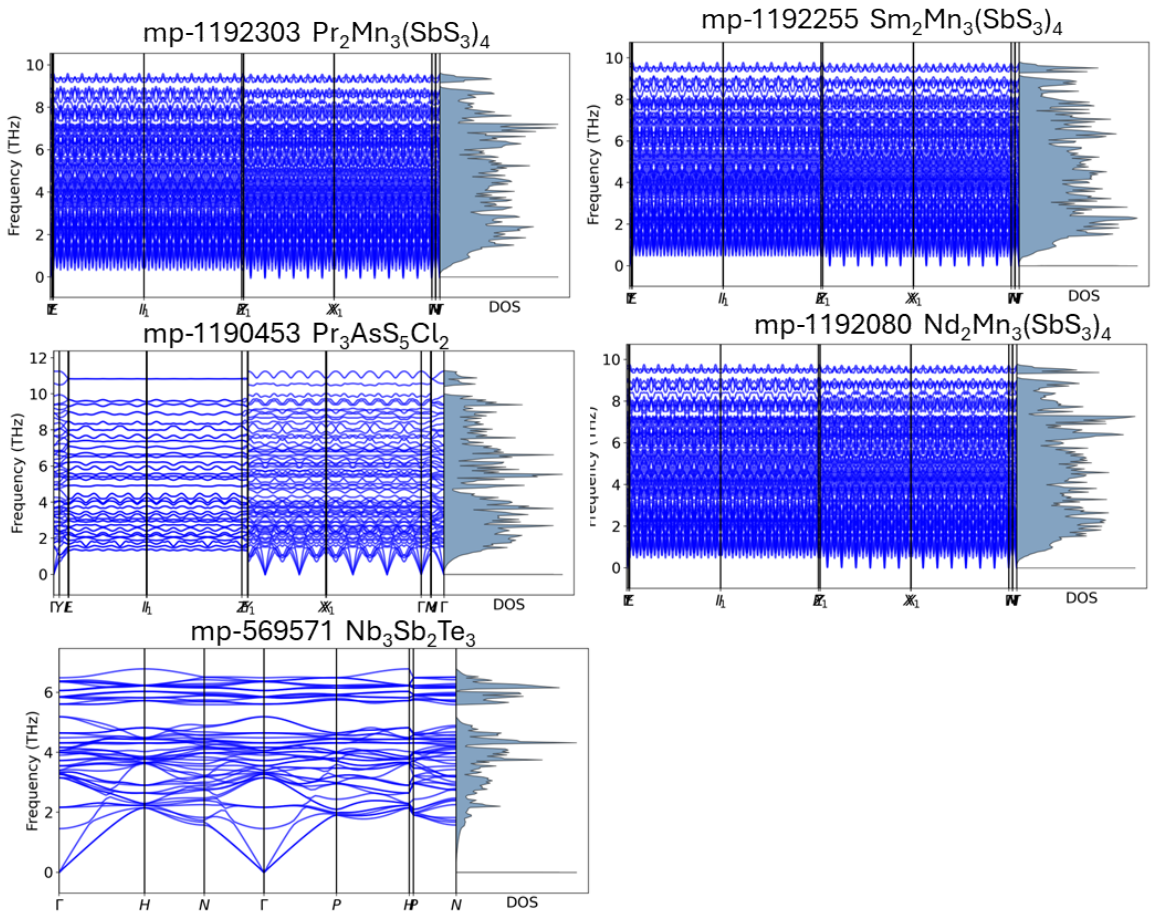

Figure S8. Phonon dispersion curves demonstrating dynamical stability of pnictogen chalcogenides from cluster C2 using MatterSim.

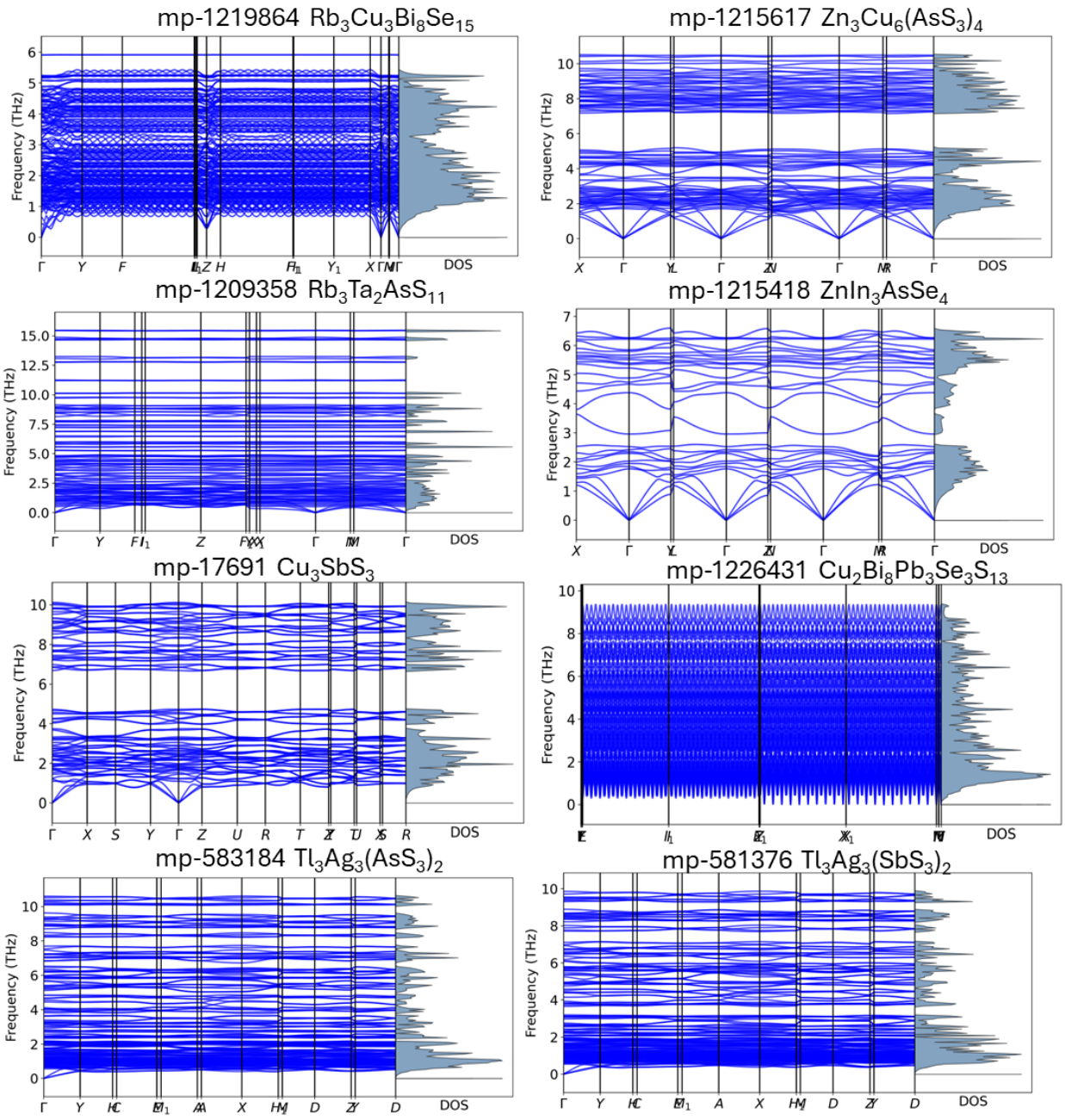

Figure S9. Phonon dispersion curves demonstrating dynamical stability of pnictogen chalcogenides from cluster C3 using MatterSim.

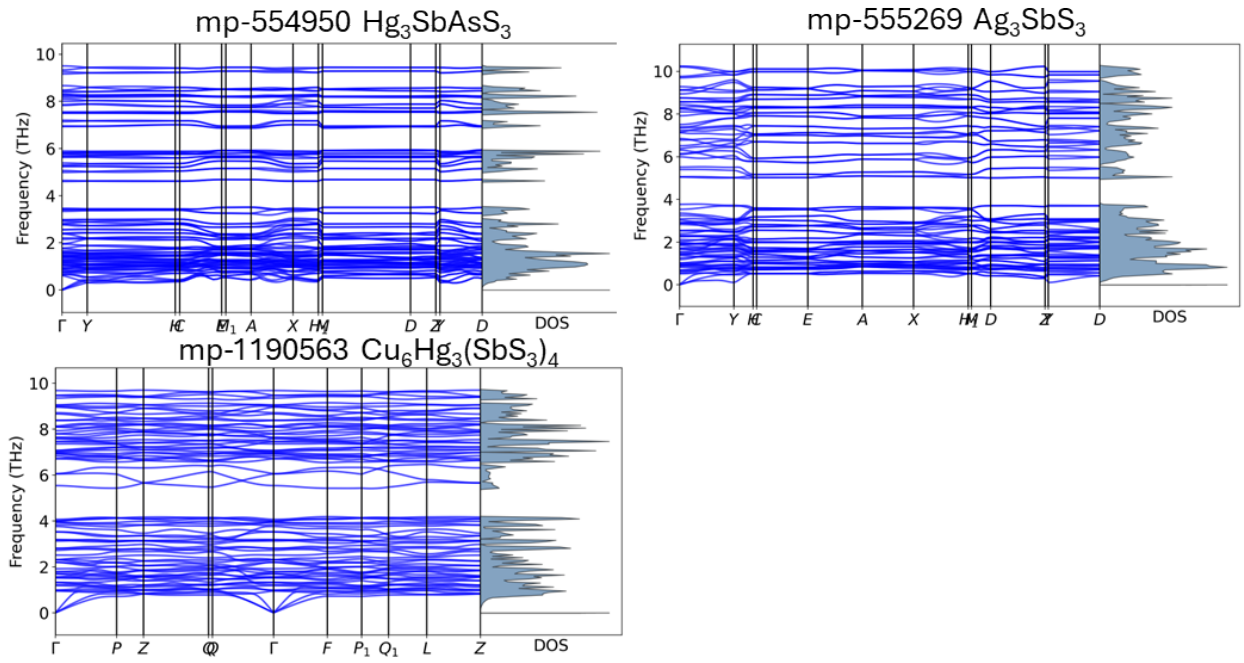

Figure S10. Phonon dispersion curves demonstrating dynamical stability of pnictogen chalcogenides from cluster C3 using MatterSim.

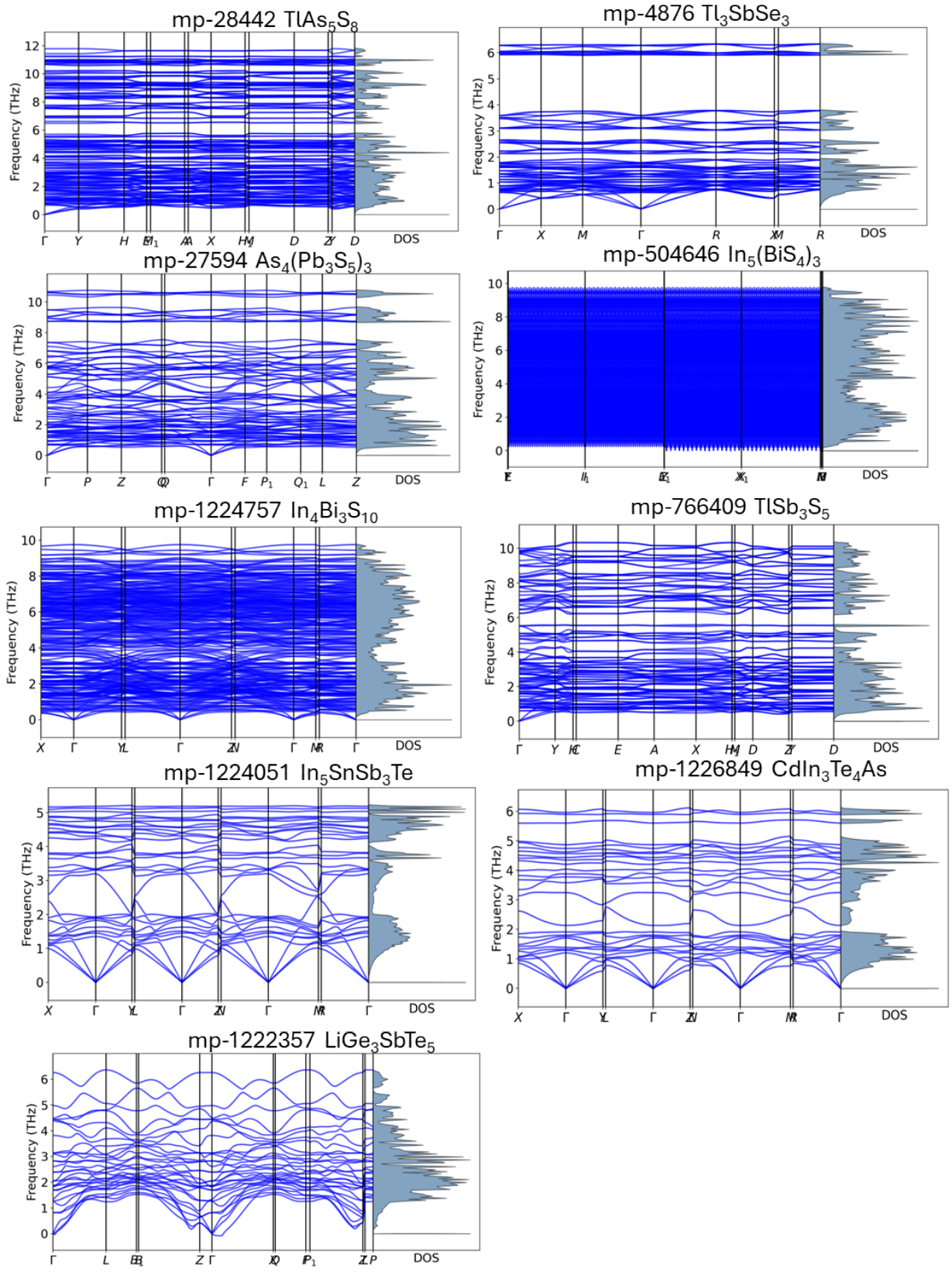

Figure S11. Phonon dispersion curves demonstrating dynamical stability of pnictogen chalcogenides from cluster C4 using MatterSim.

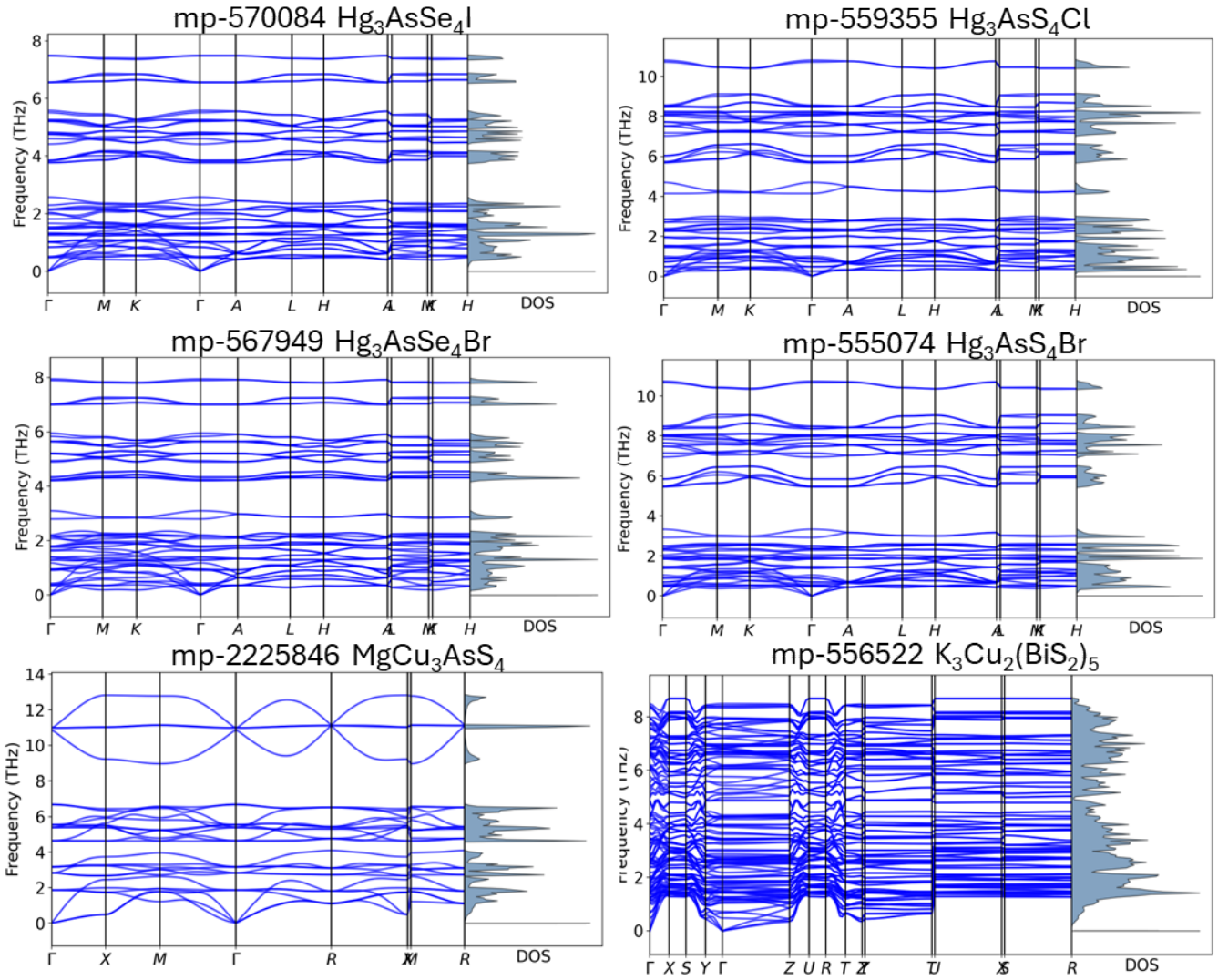

Figure S12. Phonon dispersion curves demonstrating dynamical stability of pnictogen chalcogenides from cluster C5 using MatterSim.

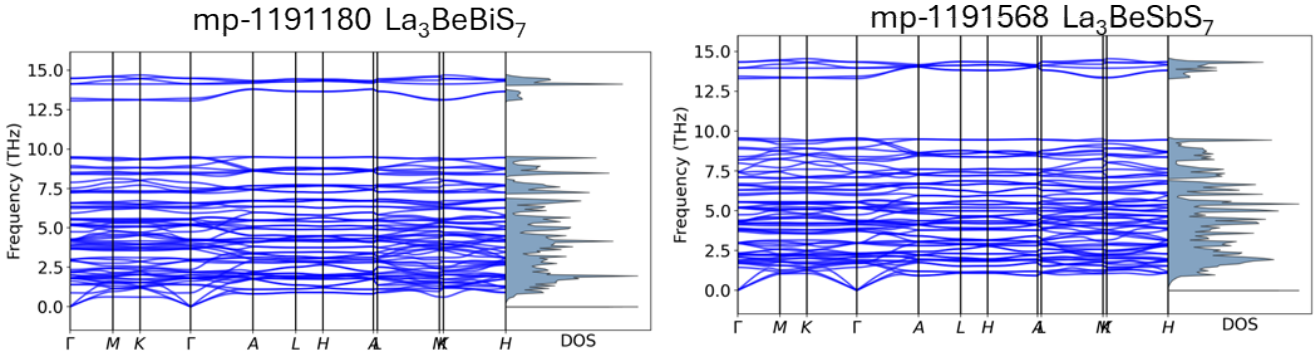

Figure S13. Phonon dispersion curves demonstrating dynamical stability of pnictogen chalcogenides from cluster C8 using MatterSim.

Table S2. Thermodynamic and electronic properties of screened pnictogen chalcogenide materials. **(a)** Energy above the convex hull (E_{Hull}) values in eV, indicating thermodynamic stability with many compounds showing values near or at 0 eV/atom. **(b)** Formation energy (E_f) in eV/atom, with all screened materials exhibiting negative values confirming their energetic favorability for synthesis. **(c)** Electronic band gap (E_g) in eV, demonstrating the semiconducting nature of the materials with gaps ranging from 0.14 to 2.60 eV, suitable for thermoelectric applications.

formula	mp_id	Energy Above Hull	Formation Energy	Band Gap
MgCu3AsS4	2225846	0.22	-0.47	0.49
CdIn3Te4As	1226849	0.01	-0.51	0.57
Cs3Sb5Se9	1226687	0.00	-0.83	0.41
Cu2Bi8Pb3Se3S13	1226431	0.01	-0.65	0.35
In4Bi3S10	1224757	0.01	-0.74	1.01
In5SnSb3Te	1224051	0.02	-0.21	0.17
KBi3S5	1223584	0.00	-0.84	1.42
LiGe3SbTe5	1222357	0.01	-0.44	0.83
Rb3Cu3Bi8Se15	1219864	0.03	-0.75	0.52
Zn3Cu6(AsS3)4	1215617	0.01	-0.58	0.68
ZnIn3AsSe4	1215418	0.00	-0.72	0.90
Rb3Ta2AsS11	1209358	0.00	-1.16	1.89
RbBi3Se5	1209327	0.00	-0.85	0.98
Cs3SbS4	1204783	0.00	-1.10	2.13
K3AsS4	1202105	0.00	-1.11	2.01
RbSb3Se5	1198114	0.00	-0.72	0.68
K3AsSe4	1197539	0.00	-1.04	1.11
Ba3Sb2S7	1195624	0.00	-1.52	1.90
Ba3Sb2Se7	1194583	0.00	-1.45	0.95
Li3SbS3	1194339	0.00	-1.17	2.40
K3SbS3	1194266	0.00	-1.15	2.70
Cs3SbS3	1193894	0.00	-1.15	2.65
Na3SbS3	1193673	0.00	-1.03	2.39
Rb3SbS3	1193319	0.00	-1.18	2.45
Na3SbSe3	1193265	0.00	-1.00	2.00
Cs3SbSe3	1192816	0.00	-1.17	2.27
Pr2Mn3(SbS3)4	1192303	0.03	-1.05	0.18
Sm2Mn3(SbS3)4	1192255	0.03	-1.05	0.14
Nd2Mn3(SbS3)4	1192080	0.03	-1.00	0.15
La3BeSbS7	1191568	0.10	-1.80	1.40
La3BeBiS7	1191180	0.11	-1.80	1.62
Cu6Hg3(SbS3)4	1190563	0.00	-0.45	0.19

Pr3AsS5Cl2	1190453	0.00	-2.03	2.16
Li3SbS3	1177520	0.04	-1.14	2.75
Li3SbS4	850275	0.07	-1.03	2.56
Li3SbS4	768269	0.06	-1.04	1.38
Li3BiS3	766409	0.07	-1.14	1.77
Li3SbS4	760415	0.00	-1.09	2.10
Li3SbS4	756316	0.00	-1.10	2.15
Li3SbS3	755463	0.04	-1.13	2.10
Li3BiS3	753720	0.03	-1.19	2.45
Li3BiS3	753677	0.05	-1.17	2.56
Li3BiS3	753444	0.07	-1.15	1.98
Ba3Bi6PbSe13	669415	0.00	-1.14	0.81
Cs3Bi7Se12	650619	0.00	-0.89	0.61
Tl3Ag3(AsS3)2	583184	0.00	-0.43	1.31
Cs3BiSe3	581738	0.00	-1.16	2.02
Tl3Ag3(SbS3)2	581376	0.00	-0.46	1.42
Hg3AsSe4I	570084	0.00	-0.46	1.22
Nb3Sb2Te5	569571	0.00	-0.64	0.84
Hg3AsSe4Br	567949	0.00	-0.52	1.30
CsBi3Se5	567928	0.00	-0.86	1.00
Hg3AsS4Cl	559355	0.00	-0.51	1.51
K3Cu2(BiS2)5	556522	0.00	-0.85	0.58
Ag3SbS3	555269	0.00	-0.21	1.51
Hg3AsS4Br	555074	0.00	-0.49	1.53
Hg3SbAsS3	554950	0.01	-0.31	1.61
In5(BiS4)3	504646	0.08	-0.69	1.43
CsBi3S5	29531	0.00	-0.86	1.43
Rb3BiSe3	29168	0.00	-1.15	2.07
K3BiSe3	28980	0.00	-1.15	2.06
Li3AsS3	28471	0.00	-1.07	2.28
TlAs5S8	28442	0.01	-0.44	1.57
As4(Pb3S5)3	27594	0.00	-0.66	1.58
TlSb3S5	27515	0.00	-0.56	1.52
K3AsSe3	18594	0.00	-1.11	2.11
Rb3AsSe4	18305	0.00	-1.06	1.31
Rb3SbSe3	17912	0.00	-1.16	2.30
Cu3SbS3	17691	0.02	-0.27	1.00
Rb3SbSe4	17638	0.00	-1.10	1.33
K3SbSe3	17538	0.00	-1.13	2.29

Rb3SbS4	17154	0.00	-1.14	2.02
Na3SbTe3	9191	0.02	-0.81	1.45
Na3AsSe3	8686	0.00	-0.96	2.01
Na3AsS3	5830	0.00	-1.01	2.52
K3SbTe3	5626	0	-0.95	1.71
Tl3SbSe3	4876	0.00	-0.44	1.01
K3AsS4	3797	0.00	-1.11	2.01

Table S3. Mean absolute errors (MAEs) for energy, forces, and stresses across screened pnictogen chalcogenide materials at final epochs. Each row corresponds to a material, and each column represents the MAE for energy, forces, and stresses on training (Train), validation (Val), and test (Test) datasets in meV, meV/Å or GPa.

mp-id_Formula	Energy			Force			Stress		
	Train	Val	Test	Train	Val	Test	Train	Val	Test
mp-1224757_In4Bi3S10	0.53	0.34	0.35	35.16	35.44	34.98	0.027	0.029	0.029
mp-1193673_Na3SbS3	0.68	0.61	0.6	23.24	23.23	23.12	0.04	0.039	0.039
mp-1192303_Pr2Mn3SbS34	1.01	1.04	1.05	36.17	36.71	36.78	0.031	0.032	0.032
mp-23474_AgBi3S5	0.72	0.63	0.65	30.92	31.02	31.22	0.032	0.033	0.033
mp-555113_Rb3Cu2BiS25	1.32	1.06	0.95	48.16	47.24	48.12	0.055	0.055	0.055
mp-1193265_Na3SbSe3	0.40	0.34	0.35	15.77	15.94	15.96	0.020	0.021	0.021
mp-2227993_Na3MgSbS4	0.36	0.27	0.32	19.89	19.79	20.18	0.014	0.015	0.014
mp-1229202_AgBi3PbS6	0.74	0.80	0.80	29.68	30.28	29.82	0.026	0.026	0.027
mp-1225886_CuBi3PbS6	0.70	0.65	0.68	36.72	37.16	37.59	0.033	0.034	0.034
mp-1194339_Li3SbS3	0.84	0.84	0.81	19.75	20.15	19.88	0.024	0.024	0.024
mp-504646_In5BiS43	0.53	0.44	0.47	31.68	32.4	31.81	0.022	0.023	0.023
mp-542302_CuBi3PbS6	0.57	0.42	0.42	40.42	40.8	41.06	0.03	0.031	0.032
mp-1229291_AgSb3PbS6	0.73	0.85	0.87	21.97	22.43	22.82	0.023	0.023	0.024
mp-1223584_KBi3S5	0.52	0.55	0.50	26.18	26.62	26.54	0.024	0.024	0.025
mp-766409_Li3BiS3	0.47	0.40	0.46	22.11	22.43	22.28	0.02	0.02	0.02
mp-9191_Na3SbTe3	0.67	0.38	0.42	22.25	21.91	22.61	0.033	0.033	0.034
mp-1227695_Bi2PbS23	0.69	0.76	0.69	32.83	32.79	33.08	0.029	0.03	0.029
mp-1194583_Ba3Sb2Se7	0.39	0.36	0.33	23.13	23.41	23.53	0.014	0.014	0.013
mp-753720_Li3BiS3	1.18	0.98	1.18	79.71	78.61	78.28	0.135	0.119	0.121
mp-17912_Rb3SbSe3	0.95	1.05	0.95	22.04	22.56	21.84	0.029	0.029	0.029
mp-1225886_CuBi3PbS6	0.70	0.64	0.68	36.72	37.15	37.58	0.032	0.034	0.034
mp-1193894_Cs3SbS3	0.15	0.14	0.14	58.53	60.73	58.92	0.052	0.062	0.090
mp-755463_Li3SbS3	1.71	1.74	1.76	20.87	20.95	21.53	0.027	0.026	0.027
mp-559356_Tl3AsS3	1.69	1.68	1.71	20.79	20.85	21.16	0.014	0.014	0.015
mp-554950_Hg3SbAsS3	1.43	1.45	1.43	20.76	20.78	0.77	0.014	0.014	0.014
mp-29295_Sr3Sb4S9	1.06	1.14	1.09	75.10	74.17	70.25	0.070	0.070	0.069
mp-2227993_Na3MgSbS4	0.35	0.27	0.31	19.78	19.78	20.18	0.014	0.014	0.014
mp-2223708_K3MgSbS4	0.28	0.28	0.25	14.05	14.21	14.30	0.013	0.013	0.013

mp-1227414_BiSbTe23	0.64	0.62	0.62	66.08	67.79	66.21	0.075	0.076	0.076

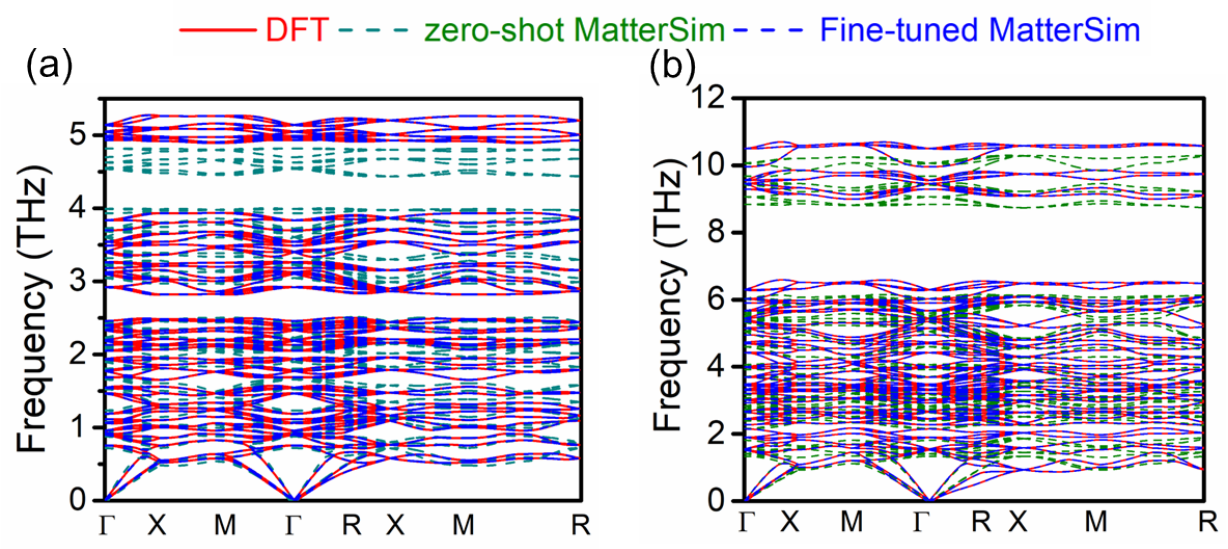

Figure S14. The phonon dispersion curves for (a) K_3SbTe_3 and (b) Na_3SbS_3 comparing density functional theory (DFT) results with predictions from MatterSim, both in its zero-shot and fine-tuned forms.

Text S3. Wigner Heat transport theory to Calculate Thermal conductivity

The Wigner formulation of heat transport provides a unified microscopic framework for describing thermal conduction across materials ranging from crystalline solids to complex/anharmonic systems.[11–13] In this formalism, the lattice thermal conductivity is expressed as the sum of two physically distinct contributions: a particle-like term associated with populations of propagating phonons, and a coherence term originating from quantum-mechanical coupling between different phonon modes.[13] This decomposition naturally extends the traditional phonon gas model (PGM) by explicitly incorporating wave-like heat conduction channels that become important in strongly anharmonic or structurally complex materials. The total conductivity is given by:

$$\kappa_{total} = \kappa_p + \kappa_c$$

where κ_p and κ_c denote the particle and coherence contributions, respectively.

1. Particle-like (Population) Contribution (κ_p)

The particle term corresponds to heat transport carried by phonon wavepackets with well-defined group velocities and finite lifetimes. It reduces exactly to the conventional solution of the Boltzmann transport equation (BTE). The expression for κ_p is:

$$\kappa_p = \frac{1}{NV}\sum_{q,s} C(q,v)v^2(q,s)\tau(q,s)$$

where N is number of sampled q-points in the Brillouin zone, V is unit-cell volume, q is phonon wavevector, s is phonon branch index, $v(q,s)$ is phonon group velocity, $\tau(q,s)$ is phonon lifetime (inverse linewidth) and $C(q,s)$ is mode-specific heat.

$$C(q,s) = \hbar\omega(q,s)\frac{dn}{dT}$$

$\omega(q,s)$ is phonon frequency, and $n(\omega)$ is Bose–Einstein population. κ_p captures the energy flow carried by phonons viewed as particles whose transport is limited by anharmonic scattering, isotopic disorder, and structural complexity. This term dominates in weakly anharmonic crystals with long phonon mean-free paths.

2. Coherence Contribution (κ_c)

The coherence contribution represents a wave-like channel of heat transport originating from off-diagonal couplings between phonon modes. This channel is absent in the classical BTE and becomes relevant when phonon linewidths are comparable to inter-mode spacings. The coherence term is:

$$\kappa_c = \frac{1}{NV}\sum_{q,s\neq s'} \frac{C(q,s)+C(q,s')}{2} v_{\alpha}^{ss'}(q)v_{\beta}^{s's}(q)\frac{2\Gamma_{ss'}(q)}{[\omega_s(q)-\omega_{s'}(q)]^2+\Gamma_{ss'}^2(q)}$$

Where, $v_{\alpha}^{ss'}(q)$ is off-diagonal velocity matrix elements coupling modes s and s′, $\Gamma_{ss'}(q)$ is combined linewidth (mode coupling strength), $\omega_s - \omega_{s'}$ is phonon frequencies of the two modes. κ_c represents heat conduction due to coherent superposition of phonon states. This channel becomes important when the structure is complex, modes are strongly hybridized, anharmonicity is strong, and phonon lifetimes are short.

Table S4. Calculated κ_L ($Wm^{-1}K^{-1}$) Values for Screened Materials at 300 K.

Formula	mp_id	κ_p^x	κ_c^x	κ_T^x	κ_p^y	κ_c^y	κ_T^y	κ_p^z	κ_c^z	κ_T^z
Li3SbS3	1177520	1.081	0.208	1.289	1.081	0.208	1.289	0.933	0.129	1.062
Pr3AsS5Cl2	1190453	0.261	0.207	0.468	0.269	0.207	0.54	0.326	0.238	0.564
Cu6Hg3(SbS3)4	1190563	1.506	0.145	1.652	1.506	0.145	1.652	1.467	0.151	1.618
La3BeBiS7	1191180	0.34	0.223	0.563	0.34	0.223	0.563	0.672	0.226	0.898
La3BeSbS7	1191568	0.549	0.218	0.768	0.549	0.218	0.768	0.899	0.216	1.116
Nd2Mn3(SbS3)4	1192080	0.522	0.326	0.849	0.151	0.228	0.379	0.29	0.251	0.542
Sm2Mn3(SbS3)4	1192255	0.379	0.32	0.699	0.129	0.243	0.372	0.199	0.261	0.46
Pr2Mn3(SbS3)4	1192303	0.494	0.327	0.821	0.143	0.228	0.371	0.289	0.255	0.544
Cs3SbSe3	1192816	0.035	0.104	0.138	0.035	0.104	0.138	0.035	0.104	0.138
Na3SbSe3	1193265	0.244	0.168	0.412	0.244	0.168	0.412	0.244	0.168	0.412
Rb3SbS3	1193319	0.092	0.108	0.2	0.092	0.108	0.2	0.092	0.108	0.2
Na3SbS3	1193673	0.12	0.239	0.358	0.12	0.239	0.358	0.12	0.239	0.358
Cs3SbS3	1193894	0.047	0.104	0.15	0.047	0.104	0.15	0.047	0.104	0.15
K3SbS3	1194266	0.075	0.146	0.221	0.075	0.146	0.221	0.075	0.146	0.221
Li3SbS3	1194339	0.696	0.314	1.01	0.538	0.258	0.796	0.733	0.339	1.072
Ba3Sb2Se7	1194583	0.034	0.149	0.182	0.044	0.158	0.202	0.048	0.155	0.203
Ba3Sb2S7	1195624	0.15	0.144	0.294	0.186	0.158	0.343	0.251	0.224	0.475
K3AsSe4	1197539	0.058	0.149	0.207	0.047	0.102	0.149	0.067	0.132	0.199
RbSb3Se5	1198114	0.375	0.408	0.783	0.126	0.226	0.352	0.13	0.254	0.384
K3AsS4	1202105	0.223	0.18	0.403	0.196	0.161	0.358	0.263	0.192	0.456
Cs3SbS4	1204783	0.012	0.108	0.12	0.009	0.083	0.092	0.011	0.103	0.114
RbBi3Se5	1209327	0.62	0.237	0.237	0.38	0.281	0.661	0.152	0.109	0.261
Rb3Ta2AsS11	1209358	0.019	0.089	0.109	0.05	0.176	0.227	0.025	0.116	0.141
ZnIn3AsSe4	1215418	0.087	0.131	0.218	0.062	0.126	0.188	0.085	0.127	0.212
Zn3Cu6(AsS3)4	1215617	6.35	0.273	6.62	6.37	0.292	6.661	6.247	0.269	6.516
Rb3Cu3Bi8Se15	1219864	0.121	0.341	0.462	0.121	0.341	0.462	0.121	0.341	0.462
LiGe3SbTe5	1222357	1.404	0.161	1.565	1.404	0.161	1.565	0.136	0.084	0.22
KBi3S5	1223584	0.414	0.445	0.859	0.107	0.24	0.347	0.115	0.272	0.387
In5SnSb3Te	1224051	4.55	0.073	4.624	4.601	0.083	4.685	4.616	0.083	4.699
In4Bi3S10	1224757	0.058	0.362	0.42	0.016	0.264	0.279	0.019	0.29	0.309
Cu2Bi8Pb3Se3S13	1226431	0.261	0.398	0.659	0.025	0.187	0.212	0.06	0.289	0.349

Cs3Sb5Se9	1226687	0.058	0.362	0.42	0.058	0.362	0.42	0.058	0.362	0.42
CdIn3Te4As	1226849	0.624	0.061	0.685	0.587	0.057	0.645	0.601	0.06	0.661
Rb3SbS4	17154	0.048	0.123	0.171	0.034	0.103	0.137	0.064	0.136	0.2
K3SbSe3	17538	0.076	0.117	0.193	0.076	0.117	0.193	0.076	0.117	0.193
Rb3SbSe4	17638	0.035	0.113	0.148	0.044	0.084	0.128	0.084	0.145	0.229
Cu3SbS3	17691	0.454	0.192	0.646	0.3	0.114	0.415	0.646	0.2	0.845
Rb3SbSe3	17912	0.121	0.111	0.232	0.121	0.111	0.232	0.121	0.111	0.232
Rb3AsSe4	18305	0.085	0.125	0.21	0.066	0.09	0.156	0.103	0.154	0.257
K3AsSe3	18594	0.022	0.138	0.16	0.022	0.138	0.16	0.022	0.138	0.16
MgCu3AsS4	2225846	0.706	0.236	0.941	0.706	0.236	0.941	0.706	0.236	0.941
TlSb3S5	27515	0.177	0.175	0.352	0.112	0.12	0.232	0.138	0.199	0.337
As4(Pb3S5)3	27594	0.069	0.315	0.384	0.069	0.315	0.384	0.058	0.243	0.301
TlAs5S8	28442	0.026	0.193	0.219	0.011	0.112	0.123	0.022	0.204	0.226
Li3AsS3	28471	0.512	0.308	0.82	0.344	0.256	0.6	0.595	0.389	0.983
K3BiSe3	28980	0.105	0.134	0.239	0.105	0.134	0.239	0.105	0.134	0.239
Rb3BiSe3	29168	0.109	0.115	0.224	0.109	0.115	0.224	0.109	0.115	0.224
CsBi3S5	29531	0.411	0.434	0.846	0.117	0.225	0.342	0.091	0.222	0.313
K3AsS4	3797	0.229	0.174	0.402	0.2	0.158	0.358	0.263	0.192	0.455
Tl3SbSe3	4876	0.03	0.098	0.129	0.03	0.098	0.129	0.03	0.098	0.129
In5(BiS4)3	504646	0.339	0.353	0.692	0.064	0.228	0.292	0.091	0.244	0.335
Hg3SbAsS3	554950	0.047	0.126	0.173	0.013	0.094	0.107	0.024	0.154	0.178
Hg3AsS4Br	555074	0.088	0.148	0.236	0.088	0.148	0.236	0.01	0.036	0.047
Ag3SbS3	555269	0.144	0.158	0.302	0.124	0.126	0.25	0.165	0.171	0.336
K3Cu2(BiS2)5	556522	0.376	0.477	0.853	0.148	0.262	0.409	0.142	0.33	0.472
Hg3AsS4Cl	559355	0.183	0.141	0.325	0.183	0.141	0.325	0.07	0.031	0.101
K3SbTe3	5626	0.063	0.094	0.157	0.063	0.094	0.157	0.063	0.094	0.157
CsBi3Se5	567928	0.546	0.236	0.783	0.343	0.272	0.615	0.153	0.111	0.264
Hg3AsSe4Br	567949	0.084	0.117	0.201	0.084	0.117	0.201	0.066	0.046	0.112
Nb3Sb2Te5	569571	1.572	0.268	1.839	1.572	0.268	1.839	1.572	0.268	1.839
Hg3AsSe4I	570084	0.088	0.115	0.202	0.088	0.115	0.202	0.02	0.036	0.056
Tl3Ag3(SbS3)2	581376	0.014	0.122	0.136	0.014	0.108	0.122	0.018	0.145	0.163
Cs3BiSe3	581738	0.034	0.114	0.149	0.034	0.114	0.149	0.034	0.114	0.149
Na3AsS3	5830	0.181	0.221	0.402	0.181	0.221	0.402	0.181	0.221	0.402
Tl3Ag3(AsS3)2	583184	0.025	0.142	0.166	0.02	0.111	0.13	0.027	0.159	0.186
Cs3Bi7Se12	650619	0.524	0.285	0.809	0.205	0.19	0.395	0.25	0.241	0.49
Ba3Bi6PbSe13	669415	0.26	0.326	0.587	0.109	0.258	0.367	0.083	0.158	0.24
Li3BiS3	753444	0.824	0.249	1.073	1.042	0.158	1.2	0.743	0.261	1.003
Li3BiS3	753677	1.641	0.199	1.84	1.641	0.199	1.84	1.929	0.227	2.157
Li3BiS3	753720	1.467	0.184	1.651	1.467	0.184	1.651	1.41	0.152	1.561
Li3SbS3	755463	1.957	0.173	2.13	1.957	0.173	2.13	2.172	0.129	2.301
Li3SbS4	756316	1.766	0.109	1.874	0.986	0.117	1.104	1.311	0.154	1.465
Li3SbS4	760415	1.657	0.106	1.763	1.657	0.106	1.763	1.431	0.089	1.52
Li3BiS3	766409	0.28	0.294	0.574	0.309	0.279	0.588	0.325	0.277	0.602
Li3SbS4	768269	0.164	0.167	0.33	0.384	0.315	0.698	0.305	0.212	0.517
Li3SbS4	850275	1.32	0.125	1.445	1.32	0.125	1.445	1.32	0.125	1.445
Na3AsSe3	8686	0.311	0.155	0.466	0.311	0.155	0.466	0.311	0.155	0.466

Na3SbTe3	9191	0.153	0.178	0.331	0.153	0.178	0.331	0.153	0.178	0.331

Text S4: Pearson correlation coefficient (PCC) analysis-based feature analysis

To understand the relationships among the features and exclude the redundant feature from the database, we employed Pearson correlation coefficients (PCCs). The PCCs is calculated to elucidate the linear relationships between various input features that influence the thermal conductivity (κ_L). The PCC is defined as:[14]

$$PCC = \frac{cov\,(x_i,x_j)}{\sigma_{x_i}\sigma_{x_j}} \quad \text{(S3)}$$

where $cov\,(x_i,x_j)$ and $\sigma_{x_{i/j}}$ are the covariance of features x_i and x_j and standard deviation of the feature $x_{i/j}$, respectively. The positive correlation indicates that both the features are in tandem and follow a linear relationship, while the negative correlation suggests that features follow inverse relations with each other.

Text S5: Description to SCALP and Non-SCALP Descriptors

The bond angle (θ) quantifies local geometrical distortions around the pnictogen centre, where compressed θ values indicate greater angular distortion, associated with enhanced SCALP activity, which amplifies lattice anharmonicity and suppresses κ_L. The lone pair distance (d_{lp}) describes the spatial extent of lone pair electron density from the pnictogen nucleus and is given by:[15]

$$d_{lp} = 3[1 + 0.0128\,(\bar{\theta} - 90)]$$

This relationship shows that enhanced lone-pair activity simultaneously alters both θ and d_{lp}, thereby modifying local bond stiffness and increasing anharmonicity.Similarly, the mismatch descriptor (δ) quantifies the disparity between the number of cations (n_{cation}) and anions (n_{anion}), defined as [16]

$$\delta = \frac{n_{cation} - n_{anion}}{n_{anion}}$$

A larger mismatch leads to increased electronic imbalance between the cation and anion orbitals, resulting in local bonding distortions that enhance phonon scattering and lower κ_L. Additionally, we introduce the electron localization function (ELF) denoted as $\rho(r)$, which exhibits a negative correlation with κ_L. It measures the spatial localization of electrons around atoms, particularly pnictogens. Higher ρ(r) indicates stronger lone pair localization, results in more asymmetric bonding environments, further enhancing phonon scattering and contributing to the reduction of κ_L.[17,18] Average polarizability of a compound is often computed as a weighted average of the atomic polarizabilities of its constituent elements. For a compound $A_xB_yC_z\cdots$with stoichiometry $x,y,z,\cdots$, the average polarizability is:

$$\grave{\alpha} = \frac{x\alpha_A + y\alpha_B + z\alpha_C + \ldots}{x + y + z + \ldots}$$

Where α_i is polarizability of element i(often taken from experimental or computed atomic polarizabilities) and x,y,z= number of atoms of each element in the formula unit.

Following the framework developed in our previous studies, we adopted two electronic structure-based descriptors to quantify bonding asymmetry: the ionicity parameter (r'_{σ}) and hybridization index (r_{π}^{-1}).[19,20] The r'_{σ} quantitatively measures the ionicity of bonds, while r_{π}^{-1} describes the extent of covalency, which can be inferred from the energetic splitting of the

s- and p-states, and their relative energy is critical for SCALP formation. These parameters are defined as:

$$r_{\sigma}^{'} = \left(\frac{\sum_i n_i r_{p,i}}{\sum_i n_i} \right) - \left(\frac{\sum_j n_j r_{p,j}}{\sum_j n_j} \right)$$

$$r_{\pi}^{-1} = \left| \left(\frac{\sum_i n_i (r_{p,i} - r_{s,i})}{\sum_i n_i} \right) - \left(\frac{\sum_j n_j (r_{p,j} - r_{s,i})}{\sum_j n_j} \right) \right| - 1$$

Here, r_p and r_s denote the valence radii of the p- and s- orbitals of atoms, summed over the i^{th} and j^{th} atoms of the material.[19,21] $r_{\sigma}^{'}$ and r_{π}^{-1} exhibit strong negative or near-zero correlations with κ_L^{avg}, implying that while they describe bond character, their direct influence on κ_L^{avg} is limited in this dataset.

Table S5. Chemical Bonding Parameters with their Average κ_L ($Wm^{-1}K^{-1}$) Values for Screened Materials at 300 K.

formula	mp_id	ELF	θ	dlp	ICOHP	ICOOP	δ	$r_{\sigma}^{'}$	r_{π}^{-1}	α	κ_L^{avg}
MgCu3AsS4	2225846	0.32	109.47	1.25	-0.71	-0.11	0.25	-0.17	2.94	5.18	0.94
CdIn3Te4As	1226849	0.25	109.46	1.25	-0.11	0.00	0.25	0.06	2.44	6.96	0.66
Cs3Sb5Se9	1226687	0.56	104.84	1.19	-0.34	0.00	-0.11	-0.21	2.38	14.47	0.42
Cu2Bi8Pb3Se3S13	1226431	0.66	103.12	1.17	-0.77	0.02	-0.19	-0.36	2.33	4.90	0.41
In4Bi3S10	1224757	0.44	95.66	1.07	-0.01	-0.29	-0.30	-0.36	2.33	5.29	0.34
In5SnSb3Te	1224051	0.75	109.46	1.25	-0.03	0.00	8.00	-0.08	2.22	8.15	4.67
KBi3S5	1223584	0.44	106.77	1.21	0.00	-0.78	-0.20	-0.36	2.33	8.90	0.53
LiGe3SbTe5	1222357	0.18	107.99	1.23	-0.03	0.00	0.00	-0.08	2.22	7.67	1.12
Rb3Cu3Bi8Se15	1219864	0.15	96.44	1.08	-0.34	0.00	-0.07	-0.26	2.13	9.59	0.46
Zn3Cu6(AsS3)4	1215617	0.22	103.53	1.17	-0.23	0.00	0.00	-0.17	2.94	4.46	6.60
ZnIn3AsSe4	1215418	0.61	109.39	1.25	-0.15	0.00	-0.55	-0.07	2.63	6.11	0.21
Rb3Ta2AsS11	1209358	0.28	100.82	1.14	-4.10	0.05	-0.45	-0.17	2.94	12.02	0.16
RbBi3Se5	1209327	0.26	103.91	1.18	-0.76	0.06	-0.20	-0.26	2.13	9.83	0.39
Cs3SbS4	1204783	0.54	109.46	1.25	-4.10	0.12	0.00	-0.31	2.63	24.63	0.11
K3AsS4	1202105	0.51	109.47	1.25	-0.09	0.00	0.00	-0.17	2.94	18.26	0.41
RbSb3Se5	1198114	0.66	104.98	1.19	-0.09	0.00	-0.20	-0.21	2.38	9.57	0.51

K3AsSe4	1197539	0.56	109.47	1.25	-0.09	0.00	0.00	-0.07	2.63	18.71	0.19
Ba3Sb2S7	1195624	0.66	96.37	1.08	-0.08	0.00	-0.29	-0.31	2.63	12.72	0.37
Ba3Sb2Se7	1194583	0.72	96.37	1.08	-1.96	0.03	-0.29	-0.21	2.38	13.24	0.20
Li3SbS3	1194339	0.73	99.25	1.12	-0.69	0.02	0.33	-0.31	2.63	12.60	0.96
K3SbS3	1194266	0.63	101.25	1.14	-0.50	0.00	0.33	-0.31	2.63	20.79	0.22
Cs3SbS3	1193894	0.66	102.57	1.16	0.00	-1.08	0.33	-0.31	2.63	27.73	0.15
Na3SbS3	1193673	0.71	99.05	1.12	0.01	-1.03	0.33	-0.31	2.63	12.30	0.36
Rb3SbS3	1193319	0.67	102.00	1.15	0.01	-1.06	0.33	-0.31	2.63	22.46	0.20
Na3SbSe3	1193265	0.74	99.63	1.12	-1.63	0.03	0.33	-0.21	2.38	12.69	0.41
Cs3SbSe3	1192816	0.62	103.08	1.17	-0.42	0.00	0.33	-0.21	2.38	28.11	0.14
Pr2Mn3(SbS3)4	1192303	0.80	102.44	1.16	-1.19	0.03	-0.25	-0.31	2.63	6.94	0.58
Sm2Mn3(SbS3)4	1192255	0.80	102.30	1.16	-1.12	0.02	-0.25	-0.31	2.63	7.00	0.51
Nd2Mn3(SbS3)4	1192080	0.40	102.48	1.16	-0.03	0.00	-0.25	-0.31	2.63	7.25	0.59
La3BeSbS7	1191568	0.46	105.82	1.20	-4.86	0.13	-0.29	-0.31	2.63	10.48	0.88
La3BeBiS7	1191180	0.78	107.27	1.22	-0.15	-0.34	-0.29	-0.36	2.33	10.55	0.67
Cu6Hg3(SbS3)4	1190563	0.19	100.59	1.14	-0.26	0.00	0.00	-0.31	2.63	4.70	1.64
Pr3AsS5Cl2	1190453	0.56	97.53	1.10	-4.58	0.17	-0.43	-0.17	2.94	9.80	0.52
Li3SbS3	1177520	0.69	99.53	1.12	-1.03	0.02	0.33	-0.31	2.63	12.60	1.21
Li3SbS4	850275	0.73	109.47	1.25	-0.25	0.00	0.00	-0.31	2.63	11.39	1.45
Li3SbS4	768269	0.73	100.16	1.13	-0.21	0.00	0.00	-0.31	2.63	11.39	0.52
Li3BiS3	766409	0.39	95.62	1.07	-0.11	-0.01	0.33	-0.36	2.33	12.71	0.59
Li3SbS4	760415	0.73	109.47	1.25	-0.12	0.00	0.00	-0.31	2.63	11.39	1.68
Li3SbS4	756316	0.74	109.47	1.25	-0.09	0.00	0.00	-0.31	2.63	11.39	1.48
Li3SbS3	755463	0.70	92.89	1.04	-0.69	0.01	0.33	-0.31	2.63	12.60	2.19
Li3BiS3	753720	0.56	106.53	1.21	0.01	-0.37	0.33	-0.36	2.33	12.71	1.62
Li3BiS3	753677	0.54	98.94	1.11	0.00	-0.85	0.33	-0.36	2.33	12.71	1.95
Li3BiS3	753444	0.62	96.25	1.08	-0.35	0.01	0.33	-0.36	2.33	12.71	1.09
Ba3Bi6PbSe13	669415	0.64	96.78	1.09	-0.04	0.00	-0.23	-0.26	2.13	9.55	0.40
Cs3Bi7Se12	650619	0.56	96.69	1.09	-0.28	0.00	-0.17	-0.26	2.13	12.55	0.56
Tl3Ag3(AsS3)2	583184	0.27	101.30	1.14	-0.19	0.00	0.33	-0.17	2.94	5.18	0.16
Cs3BiSe3	581738	0.63	102.67	1.16	-0.39	0.00	0.33	-0.26	2.13	28.23	0.15
Tl3Ag3(SbS3)2	581376	0.72	99.16	1.12	-3.47	-0.14	0.33	-0.31	2.63	5.51	0.14
Hg3AsSe4I	570084	0.65	94.22	1.05	-0.06	0.00	-0.20	-0.07	2.63	4.52	0.15
Nb3Sb2Te5	569571	0.25	109.45	1.25	-1.55	-0.11	0.00	-0.08	2.22	8.78	1.84
Hg3AsSe4Br	567949	0.63	93.10	1.04	-0.06	0.00	-0.20	-0.07	2.63	4.31	0.17
CsBi3Se5	567928	0.56	103.98	1.18	-0.20	0.00	-0.20	-0.26	2.13	11.20	0.55
Hg3AsS4Cl	559355	0.64	94.39	1.06	-2.12	0.03	-0.20	-0.17	2.94	3.81	0.25
K3Cu2(BiS2)5	556522	0.18	105.94	1.20	-0.14	0.00	0.00	-0.36	2.33	10.48	0.58
Ag3SbS3	555269	0.62	96.56	1.08	-0.20	0.00	0.33	-0.31	2.63	5.57	0.30
Hg3AsS4Br	555074	0.58	94.93	1.06	-0.08	0.00	-0.20	-0.17	2.94	3.91	0.17
Hg3SbAsS3	554950	0.66	96.30	1.08	0.00	-1.05	0.67	-0.31	2.63	4.48	0.15
In5(BiS4)3	504646	0.37	96.29	1.08	0.03	-0.69	-0.42	-0.36	2.33	5.28	0.44
CsBi3S5	29531	0.43	105.76	1.20	0.00	-0.52	-0.20	-0.36	2.33	10.70	0.50
Rb3BiSe3	29168	0.31	101.57	1.15	-0.76	0.03	0.33	-0.26	2.13	22.96	0.22
K3BiSe3	28980	0.22	100.60	1.14	-0.92	0.02	0.33	-0.26	2.13	21.29	0.24
Li3AsS3	28471	0.63	102.22	1.16	-0.90	0.16	0.33	-0.17	2.94	12.27	0.80

TlAs5S8	28442	0.59	96.76	1.09	-0.07	0.00	-0.25	-0.17	2.94	3.74	0.19
As4(Pb3S5)3	27594	0.66	99.61	1.12	-0.07	0.00	-0.20	-0.17	2.94	4.35	0.36
TlSb3S5	27515	0.69	99.27	1.12	-0.03	0.00	-0.20	-0.31	2.63	4.66	0.31
K3AsSe3	18594	0.62	104.26	1.18	-0.52	0.00	0.33	-0.07	2.63	20.84	0.16
Rb3AsSe4	18305	0.53	109.46	1.25	-0.11	0.00	0.00	-0.07	2.63	20.17	0.21
Rb3SbSe3	17912	0.72	102.50	1.16	-3.76	0.17	0.33	-0.21	2.38	22.84	0.23
Cu3SbS3	17691	0.64	98.28	1.11	-0.17	0.00	0.33	-0.31	2.63	5.06	0.64
Rb3SbSe4	17638	0.60	109.46	1.25	-0.14	0.00	0.00	-0.21	2.38	20.46	0.17
K3SbSe3	17538	0.69	101.68	1.15	-0.52	0.00	0.33	-0.21	2.38	21.17	0.19
Rb3SbS4	17154	0.56	109.46	1.25	-0.16	0.00	0.00	-0.31	2.63	20.01	0.17
Na3SbTe3	9191	0.80	99.58	1.12	-3.04	0.13	0.33	-0.08	2.22	13.41	0.33
Na3AsSe3	8686	0.67	102.58	1.16	-0.71	0.00	0.33	-0.07	2.63	12.36	0.47
Na3AsS3	5830	0.62	102.18	1.16	-0.24	0.00	0.33	-0.17	2.94	11.97	0.40
K3SbTe3	5626	0.72	102.49	1.16	-3.23	0.15	0.33	-0.08	2.22	21.90	0.16
Tl3SbSe3	4876	0.70	100.58	1.14	-0.09	0.00	0.33	-0.21	2.38	5.83	0.13
K3AsS4	3797	0.50	109.47	1.25	-0.08	0.00	0.00	-0.17	2.94	18.26	0.41

Table S6. Chemical Bonding Descriptor Correlations highlighting the SCALP and Structural Distortion mechanisms influencing κ_L

Mechanism	**Chemical Bonding Descriptor Design**	**Correlation Coefficient**	**Parameters**
SCALP	$\frac{ICOHP \times ICOHP(s)}{ICOOP(p)}$	0.38	ICOHP/ICOOP (s/p)
SCALP	$ICOHP(s) \times cos(ICOHP)$	0.36	ICOHP (s)
SCALP	$cbrt(ICOHP(s) \times ICOOP(s))$	0.35	ICOHP/ICOOP (s)
SCALP	$ICOHP(s) \times (ICOOP(s))^2$	0.34	ICOHP/ICOOP (s)
Structural Distortion	$cos(sqrt(\alpha))$	0.58	α
Structural Distortion	$abs((\alpha) - sqrt(\theta))$	0.54	α, θ
Structural Distortion	$((\delta + \theta) - \alpha)$	0.46	δ, θ, α
Structural Distortion	$((ICOHP + \theta) - \alpha)$	0.46	$ICOHP$, θ, α
SCALP + Structural Distortion	$(ICOHP - \alpha)^3$	0.45	$ICOHP$, α

Structural Distortion	$((r_{\pi}^{-1} + \alpha) - \theta)$	0.45	$r_{\pi}^{-1}, \alpha, \theta$

*abs=absolute value function; cbrt=cube root function; cos/sin=trigonometric functions; exp=exponential function

References

(1) Ward, L.; Dunn, A.; Faghaninia, A.; Zimmermann, N. E. R.; Bajaj, S.; Wang, Q.; Montoya, J.; Chen, J.; Bystrom, K.; Dylla, M.; Chard, K.; Asta, M.; Persson, K. A.; Snyder, G. J.; Foster, I.; Jain, A. Matminer: An Open Source Toolkit for Materials Data Mining. *Comput Mater Sci* **2018**, *152*. https://doi.org/10.1016/j.commatsci.2018.05.018.

(2) Abdi, H.; Williams, L. J. Principal Component Analysis. *Wiley Interdisciplinary Reviews: Computational Statistics*. 2010. https://doi.org/10.1002/wics.101.

(3) Tang, J.; Liu, J.; Zhang, M.; Mei, Q. Visualizing Large-Scale and High-Dimensional Data. In *25th International World Wide Web Conference, WWW 2016*; 2016. https://doi.org/10.1145/2872427.288304l.

(4) Sinaga, K. P.; Yang, M. S. Unsupervised K-Means Clustering Algorithm. *IEEE Access* **2020**, *8*. https://doi.org/10.1109/ACCESS.2020.2988796.

(5) Yang, H.; Hu, C.; Zhou, Y.; Liu, X.; Shi, Y.; Li, J.; Li, G.; Chen, Z.; Chen, S.; Zeni, C.; Horton, M.; Pinsler, R.; Fowler, A.; Zügner, D.; Xie, T.; Smith, J.; Sun, L.; Wang, Q.; Kong, L.; Liu, C.; Hao, H.; Lu, Z. MatterSim: A Deep Learning Atomistic Model Across Elements, Temperatures and Pressures. **2024**.

(6) Batatia, I.; Kovács, D. P.; Simm, G. N. C.; Ortner, C.; Csányi, G. MACE: Higher Order Equivariant Message Passing Neural Networks for Fast and Accurate Force Fields. **2023**.

(7) Deng, B.; Zhong, P.; Jun, K. J.; Riebesell, J.; Han, K.; Bartel, C. J.; Ceder, G. CHGNet as a Pretrained Universal Neural Network Potential for Charge-Informed Atomistic Modelling. *Nat Mach Intell* **2023**, *5* (9). https://doi.org/10.1038/s42256-023-00716-3.

(8) Lee, J.; Asahi, R. Transfer Learning for Materials Informatics Using Crystal Graph Convolutional Neural Network. *Comput Mater Sci* **2021**, *190*. https://doi.org/10.1016/j.commatsci.2021.110314.

(9) Chen, C.; Ong, S. P. AtomSets as a Hierarchical Transfer Learning Framework for Small and Large Materials Datasets. *NPJ Comput Mater* **2021**, *7* (1). https://doi.org/10.1038/s41524-021-00639-w.

(10) Wang, R.; Zou, Y.; Zhang, C.; Wang, X.; Yang, M.; Xu, D. Combining Crystal Graphs and Domain Knowledge in Machine Learning to Predict Metal-Organic Frameworks Performance in Methane Adsorption. *Microporous and Mesoporous Materials* **2022**, *331*. https://doi.org/10.1016/j.micromeso.2021.111666.

(11) Simoncelli, M.; Marzari, N.; Mauri, F. Unified Theory of Thermal Transport in Crystals and Glasses. *Nat Phys* **2019**, *15* (8). https://doi.org/10.1038/s41567-019-0520-x.

(12) Isaeva, L.; Barbalinardo, G.; Donadio, D.; Baroni, S. Modeling Heat Transport in Crystals and Glasses from a Unified Lattice-Dynamical Approach. *Nat Commun* **2019**, *10* (1). https://doi.org/10.1038/s41467-019-11572-4.

(13) Simoncelli, M.; Marzari, N.; Mauri, F. Wigner Formulation of Thermal Transport in Solids. *Phys Rev X* **2022**, *12* (4). https://doi.org/10.1103/PhysRevX.12.041011.

(14) Zhou, H.; Deng, Z.; Xia, Y.; Fu, M. A New Sampling Method in Particle Filter Based on Pearson Correlation Coefficient. *Neurocomputing* **2016**, *216*. https://doi.org/10.1016/j.neucom.2016.07.036.

(15) Skoug, E. J.; Morelli, D. T. Role of Lone-Pair Electrons in Producing Minimum Thermal Conductivity in Nitrogen-Group Chalcogenide Compounds. *Phys Rev Lett* **2011**, *107* (23). https://doi.org/10.1103/PhysRevLett.107.235901.

(16) Deng, T.; Wei, T. R.; Huang, H.; Song, Q.; Zhao, K.; Qiu, P.; Yang, J.; Chen, L.; Shi, X. Number Mismatch between Cations and Anions as an Indicator for Low Lattice Thermal Conductivity in Chalcogenides. *NPJ Comput Mater* **2020**, *6* (1). https://doi.org/10.1038/s41524-020-00355-x.

(17) Becke, A. D.; Edgecombe, K. E. A Simple Measure of Electron Localization in Atomic and Molecular Systems. *J Chem Phys* **1990**, *92* (9). https://doi.org/10.1063/1.458517.

(18) Silvi, B.; Savin, A. Classification of Chemical Bonds Based on Topological Analysis of Electron Localization Functions. *Nature* **1994**, *371* (6499). https://doi.org/10.1038/371683a0.

(19) Lencer, D.; Salinga, M.; Grabowski, B.; Hickel, T.; Neugebauer, J.; Wuttig, M. A Map for Phase-Change Materials. *Nat Mater* **2008**, *7* (12). https://doi.org/10.1038/nmat2330.

(20) Minhas, H.; Jena, M. K.; Sharma, R. K.; Pathak, B. Insights into Thermal Conductivity of Pnictogen Chalcogenides: Machine Learning Stereochemically Active Lone Pairs and Hybridization. *Chemistry of Materials* **2024**. https://doi.org/10.1021/acs.chemmater.4c02294.

(21) Chelikowsky, J. R.; Phillips, J. C. Quantum-Defect Theory of Heats of Formation and Structural Transition Energies of Liquid and Solid Simple Metal Alloys and Compounds. *Phys Rev B* **1978**, *17* (6). https://doi.org/10.1103/PhysRevB.17.2453.